Nuclear quantum effects in solid water: new insights from computational modeling

Rasti, S.

CHAPTER 4

Calorimetric Signature of Deuterated Ice II

This chapter is based on:

V. Fuentes-Landete, S. Rasti, R. Schlögl, J. Meyer and T. Loerting, Calorimetric Signature of Deuterated Ice II: Turning an Endotherm to an Exotherm, *J. Phys. Chem. Lett.* **11**, 8268 (2020).

Abstract

Calorimetric studies on ice II reveal a surprising H_2O/D_2O isotope effect. While the ice II to ice Ic transition is endothermic for H_2O, it is exothermic for D_2O samples. The transition enthalpies are $+40\,\mathrm{J\,mol^{-1}}$ and $-140\,\mathrm{J\,mol^{-1}}$, respectively, where such a sign change upon isotope substitution is unprecedented in ice research. In order to understand the observations, force field calculations are employed using two water models known to perform well for H_2O ice phases and their vibrational properties. These simulations reveal that the isotope effect can be traced back to zero-point energy. q-TIP4P/F fares better and is able to account for about 3/4 of the isotope effect, while MB-pol only catches about 1/3. Phonon and configurational entropy contributions are necessary to predict reasonable transition enthalpies, but do not have an impact on the isotope effect. This study suggests to use these calorimetric isotope data as benchmark for water model.

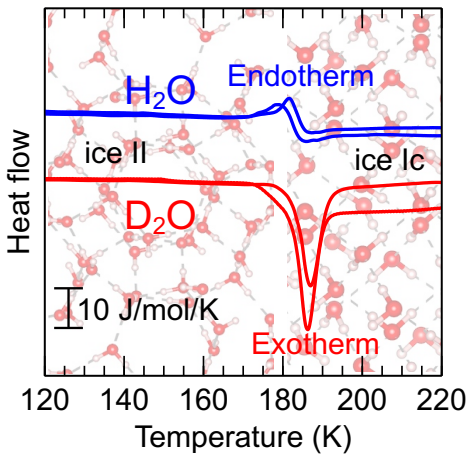

4.1 Introduction

The first high-pressure form of ice, ice II, was discovered in 1900 by Tammann [1]. In the 1960s the structure of ice II has been determined to be hydrogen-ordered [2–

5]. Within the framework of the Bernal-Fowler rules [6] ice II is a phase of zero configurational entropy, where configurational entropy is solely based on the number of microstates differing in terms of H-atom positions. By contrast, hexagonal ice (ice Ih) is geometrically frustrated, showing a disordered network of H atoms. Ice Ih is hence a phase of non-zero configurational entropy. In fact, ice II is thermodynamically more stable than hexagonal ice even at ambient pressure because the entropy of ice Ih is smaller at low temperatures. The idea that the high-pressure phase ice II is the ground state at 0 K and ambient pressure had to be abandoned years later, after the discovery of the hydrogen-ordered counterpart of hexagonal ice, ice XI [7]. In 1963 Bertie, Calvert and Whalley examined the transformations that occur when heating high-pressure ices from liquid nitrogen temperatures at ambient pressure [8]. The thermal analysis was made by using a small silvered-glass vacuum flask as a calorimeter. The heating curve of ice II shows a small break in the heat capacity around 170 to 175 K. Two possible interpretations consistent with the observations were given: (i) A first-order phase transition involving an undetectably small heat, but associated with a large decrease of heat capacity, and (ii) a continuous transition involving decrease in heat capacity. 25 years later, in 1988, Handa and Klug [9] demonstrated that actually interpretation (i) is correct, by detecting the heat involved in the transition to cubic ice (ice Ic). They reported a weak endotherm when heating ice II in their Tian-Calvet calorimeter at $10\,\mathrm{K\,h^{-1}}$ with an onset temperature at 161 K and enthalpy of transformation (ΔH) of $+54 \pm 5\,\mathrm{J\,mol^{-1}}$ [9]. That makes ice II the only example of a high-pressure ice converting endothermically to ice Ic at 1 bar. For comparison other high-pressure ice phases such as ice V, ice VI or ice XII show pronounced exotherms of $-926 \pm 20\,\mathrm{J\,mol^{-1}}$ [10], $-1523 \pm 16\,\mathrm{J\,mol^{-1}}$ [11] and $-1233 \pm 23\,\mathrm{J\,mol^{-1}}$ [12], respectively.

This is explained by taking into account that the heat of transformation is composed of two contributions. The first contribution is an enthalpic term arising from the transformation from high density (ice II) to low density (ice Ic). The restructuring from ice II to ice Ic involves a density change from $1.21\,\mathrm{g/cm^3}$ to $0.94\,\mathrm{g/cm^3}$ [13]. In spite of this 22 % density decrease, the structural motif of hexagonal channels is conserved. Up to 7/12 of all hydrogen bonds are retained at the irreversible cooperative II $\rightarrow$ Ic

transition [14]. Just like for all other high-pressure ice phases this enthalpic term is exothermic [9]. The second contribution is an entropic term arising from the transformation of hydrogen-ordered (ice II) to hydrogen-disordered (ice Ic). This change in the H-atom subnetwork is also responsible for the increase in heat capacity observed in the calorimetry scans - the number of degrees of freedom and hence heat capacity is smaller in an H-ordered ice. This entropic term is endothermic, just like for all disordering transformations, e.g., melting. In sum the two contributions result in a very weak overall endotherm associated with the ice II $\rightarrow$ ice Ic transformation at 1 bar. By contrast, ices V, VI and XII are all hydrogen-disordered. On their phase transitions to hydrogen-disordered ice Ic only the enthalpic term plays a role, but not the entropic term. The presence of both terms makes the ice II $\rightarrow$ ice Ic transition a particularly challenging case, also of great interest for simulations and benchmarking water models. Studies with deuterated samples are of high importance since these are required to deduce the crystal structure from neutron diffraction data. The thermal behavior of several deuterated ice samples has been investigated by differential scanning calorimetry [11, 12, 15–17]. Deuteration usually translates into a more exothermic transformation to ice Ic. Specifically, the exotherm increases by 107 and 175 $\mathrm{J\,mol^{-1}}$ after deuteration of ices VI and XII, respectively [11, 12]. Although ice II was discovered more than a century ago, no calorimetric data for D_2O ice II have been available up to now. This chapter reports the thermal behavior of recovered D_2O ice II and compare it with the one for H_2O. Our study reveals an exothermic ice II to ice Ic transition for D_2O, contrary to the endothermic nature for H_2O. This represents the first example in which the calorimetric signature changes from endothermic to exothermic upon deuteration. To rationalize these findings the transition is analyzed based on lattice energy and phonon calculations.

4.2 Methods

4.2.1 Experimental Methods

The ice II samples were prepared in the piston-cylinder apparatus by using a computerized universal testing machine (Zwick, model BZ100/TL3S). This study used 600 µL of H_2O or D_2O, which were pipetted into an indium container inside the high-pressure apparatus for compression. Indium containers were employed to avoid unwanted pressure drops during experiments [18]. Two different protocols were followed for the preparation of ice II samples. The first protocol is taken from Bauer *et al.* [19] and consists of the direct polymorphic transformation of ice Ih to ice II by slow compression to 0.40 GPa at 198 K. The rather low compression rate of 10 MPa min^{-1} between 0.20 to 0.40 GPa ensures that no parallel polymorphic transformation takes place [19]. The second protocol used to produce ice II is adapted from the work of Salzmann *et al.* [20]. By heating ice Ih at 0.50 GPa, a chain of polymorphic transformations to ice III, ice II and ice V takes place up to $\sim$ 250 K. By isobaric heating of Ih at 0.50 GPa to $\sim$ 200 K ice II is obtained.

In both routes the pressurized ice II sample is then quenched in liquid nitrogen, and the pressure released to recover ice II at ambient pressure. No transformations take place upon quench-recovery. In spite of hexagonal ice being the stable phase at 77 K, no transformation back to hexagonal ice takes place while storing the sample at ambient pressure and 77 K. At 77 K the kinetics of O-atom restructuring is immeasurably slow. The restructuring of the network of O atoms only proceeds at measurable rates above about 150 K.

Typically, a mass of 10 to 20 mg was cut from the cylindrical ice II sample of 600 mg in total. The grains of ice II were then transferred under liquid nitrogen into an aluminum crucible and covered with a lid. These crucibles were cold loaded into our differential scanning calorimeter (DSC 8000 Perkin Elmer) and subsequently heated two times at 30 K min^{-1}. The first scan, heated to 253 K, shows the polymorphic transitions first to ice Ic and ultimately yielding hexagonal ice Ih. The second one, to 313 K, shows

the endotherm due to the melting of hexagonal ice Ih. From the melting peak the mass of the sample have been calculated based on the known heat of fusion of D_2O, $6280\,\mathrm{J\,mol^{-1}}$ [21] (or $6012\,\mathrm{J\,mol^{-1}}$ in case of H_2O). All calorimetry scans were recorded at ambient pressure. This procedure is identical to the established procedure reported in earlier work from Gasser *et al.* [22] and Fuentes-Landete *et al.* [23, 24]

4.2.2 Computational Details

The computational setup is almost identical to the one used in Chapter 3. Briefly, the q-TIP4P/F water model [25] has been evaluated using the Atomic Simulation Environment (ASE) [26] with the LAMMPS code [27] via the available calculator, whereas a new calculator has been implemented in order to interface with the MB-pol model[1] as developed and implemented by the Paesani group [28–30]. Data obtained from neutron diffraction experiments [31, 32] has been used with the GENICE package [33] in order to generate the initial structures of ice II and I.

ASE is employed for all geometry optimizations[2] with a tight maximum force threshold of $10^{-4}\,\mathrm{eV\,\AA^{-1}}$. Vibrational properties have been calculated for the different ice phases based on the Parlinski-Li-Kawazoe finite-displacement method [35] (using displacements of $10^{-3}\,\mathrm{\AA}$) as implemented in the PHONOPY package [36]. Very tight $30\times30\times30$ reciprocal space grids have been used for the evaluation of Eq. (4.5), resulting in at

[1] MB-pol calculations are based on an in-house ASE-calculator building on the MB-pol plugin for OpenMM (Release 1.1.2), available from the Paesani group (`https://github.com/paesanilab/mbpol_openmm_plugin`). This implementation can only handle periodic boundary conditions for orthogonal cells of a certain minimum size. For this reason, a 3x3x3 (3x2x7) supercell of ice Ih (ice II) has been constructed internally in our ASE-MB-pol calculator.

[2] The calculations reported here are based on structure optimizations that do not constrain the space group. The structure optimizations have also been repeated for ice Ih using the in-house space-group constraint (SPGC) discussed in more details in Chapter 3. Briefly, in order to simultaneous relax the lattice vectors and the internal coordinates of each ice structure while constraining its space group, the algorithm suggested by Pfrommer *et al.* [34] has been implemented into the Atomic Simulation Environment (ASE) [26]. At Tables 4.5 and 4.6, the results were compared from these calculations to the corresponding ones in Tables 4.2 and 4.3

least 1456 points in the irreducible wedge of the Brillouin zone for which vibrational frequencies have been calculated. In these calculations, ice Ih has been used in place of ice Ic since these two ice phases are energetically almost degenerate, with hexagonal ice being more stable by a margin close to zero, even difficult to measure in calorimetry scans. Fig. 4.1 shows a very small baseline change near 210 K that corresponds to the ice Ic to ice Ih transition - this exotherm is smaller than 10 J/mol and negligible in the present context. Engel *et al.* [37] have suggested that the proper energetic ordering of ices Ih and Ic can only be described by taking anharmonic affects into account, which is beyond the scope of the present work. Furthermore, ice Ic and ice Ih have almost indistinguishable spectral properties from the microwave to the ultraviolet. For this reason they are commonly both denoted as ice I, where the difference between ice Ic and ice Ih is the stacking-sequence. Specifically, all vibrational transitions have long been thought to be identical for ice Ic and ice Ih [38]. Also the intermolecular phonon modes in the far-infrared spectral range barely reveal any difference. [39, 40] Subtle differences based on different polytypes of ice Ih containing different hexagonal and cubic stacking sequences have only been noted recently by Carr *et al.* [41]. In a very recent work the transition from a pure cubic stacking sequence to a pure hexagonal stacking sequence was identified, where only very small shifts, e.g., of about $2\,\mathrm{cm}^{-1}$ in the translational band mark the transition [42].

4.3 Results and Discussion

4.3.1 Experiments

Figure 4.1 shows the representative scans of ice II for H_2O and D_2O. For each isotopologue two different scans are reported which correspond to the two distinct routes followed for preparation of the ice II samples (for details see "Computational details" above). The H_2O calorimetric signature represented here in blue agrees well with the one published by Handa and Klug [9]. Table 4.1 shows the enthalpy and onset values for the ice II to ice Ic transition calculated in this study. Note that the heating rate

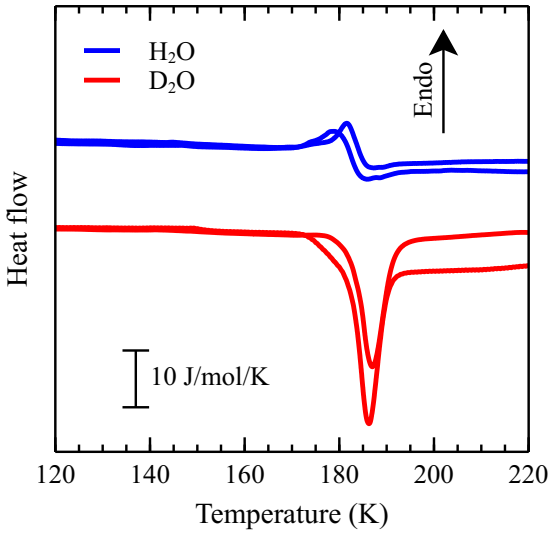

Figure 4.1: DSC heating scans recorded at $30\,\mathrm{K\,min^{-1}}$ and ambient pressure for H_2O (blue) and D_2O (red) ice II. The signal is normalized to 1 mol.

employed by Handa and Klug [9] is $10\,\mathrm{K\,h^{-1}}$ while here $30\,\mathrm{K\,min^{-1}}$ is employed, thus explaining the onset temperature shift of about $\sim 10\,\mathrm{K}$. The D_2O scans in Fig. 4.1 in red represent the first measurements for deuterated ice II shown in literature. The exothermic nature of this transition can be easily recognized. Whereas the transition is endothermic for the two preparation protocols for H_2O ($+33 \pm 11\,\mathrm{J\,mol^{-1}}$ and $+48 \pm 9\,\mathrm{J\,mol^{-1}}$, respectively), it is exothermic for D_2O ice II ($-132 \pm 36\,\mathrm{J\,mol^{-1}}$ and $-149 \pm 50\,\mathrm{J\,mol^{-1}}$, respectively) [19, 20]. That is, the ice II $\rightarrow$ ice Ic transition is more exothermic by about $180 \pm 20\,\mathrm{J\,mol^{-1}}$ in D_2O than in H_2O. In the present work, the enthalpy values are averages of at least ten different scans for each preparation route. In Fig. 4.1, only one representative DSC scan is shown. This isotope effect on the enthalpy difference to ice Ic is not unusual. Similar differences were found for other high-pressure polymorphs, too. As mentioned above, the transition from ice XII to Ic is about $175\,\mathrm{J\,mol^{-1}}$ more exothermic for D_2O than for H_2O[12].

In addition, the onset temperatures for the transition in hydrogenated and deuterated

samples are shown in Table 4.1. The difference in onsets is 7 to 10 K. This is substantially more than the usual difference between structural transitions in H_2O and D_2O. For instance, all the triple points in the phase diagram are higher in D_2O than in H_2O by between 2.2 K (for the liquid-ice V-ice VI triple point) and 3.8 K (for the liquid-ice Ih-gas triple point) [43, 44]. By contrast, dynamic transitions have larger isotope effects. D_2O–H_2O isotope effects of 6 to 8 K were found for the orientational glass transitions in the H-subnetwork of ices IV, V, VI and XII [24]. This suggests that dynamics plays a crucial role for the ice II $\rightarrow$ ice Ic transition as well. While it is H-atom dynamics in case of the orientational glass transitions, this study here measures the isotope effect on the O-atom restructuring. This restructuring takes place in an out-of-equilibrium situation, since ice II is kinetically stable at 77 K and 1 bar, but not thermodynamically. Similarly, also for the case of the ice XII $\rightarrow$ ice Ic and ice IV $\rightarrow$ ice Ic transitions the isotope effect on the onset temperature amounts to 7 ± 1 K at heating rates of 30 K min^{-1} [12]. Reducing the heating rate to 5 K min^{-1} the isotope effect is reduced to 4 ± 1 K [12]. That is, the onset temperature of the transition is kinetically controlled.

4.3.2 Calculations

In order to better understand the observed isotope effect on the transition enthalpy, calculations with two different water models have been performed, q-TIP4P/F [25] and MB-pol [28–30]. Both of them involve flexible water molecules, which allow to calculate vibrational properties including all inter- and intramolecular contributions. It is found in previous work that including zero-point energy (ZPE) with q-TIP4P/F provides a very good description of experimental data for a plethora of different crystalline ice phases – outperforming several density functionals despite its simplicity [45]. This study has also included the state-of-the-art polarizable many-body force field MB-pol given its excellent description of vibrational properties of ice [46, 47].

Periodic boundary conditions have been used in order to model the different ice phases and relax the structures while constraining the space group symmetry as suggested

by Pfrommer *et al.* [34]. Absolute lattice energies $E_{\rm lat}$ are calculated as differences of total energies between the ice phase with $N_{\rm ice}$ molecules in the unit cell after relaxation ($E_{\rm ice}$) and the corresponding constituent molecules at infinite separation ($E_{\rm mol}$)

$$E_{\rm lat} = \frac{1}{N_{\rm ice}} E_{\rm ice} - E_{\rm mol} \; . \tag{4.1}$$

Calculating vibrational frequencies then allows to include the missing ZPE effects according to

$$E_{\rm lat}^{\rm ZPE} = \frac{1}{N_{\rm ice}} (E_{\rm ice} + E_{\rm ice}^{\rm ZPE}) - (E_{\rm mol} + E_{\rm mol}^{\rm ZPE}) \tag{4.2}$$

In order to compare with the measured enthalpies for the ice II $\rightarrow$ Ic transition and analyze the isotope effect, the following (free) energy differences has been considered, decreasing the number of approximations in each step:

1. Our starting point is the lattice energy difference

$$\Delta E_{\rm lat} = E_{\rm lat}({\rm I}) - E_{\rm lat}({\rm II}) \, , \tag{4.3}$$

   which is of course identical for H_2O and D_2O.

2. Isotope effects at $T = 0\,{\rm K}$ are accounted for when including the (slightly) different ZPE corrections to the lattice energies for each ice phase

$$\Delta E_{\rm lat}^{\rm ZPE} = E_{\rm lat}^{\rm ZPE}({\rm I}) - E_{\rm lat}^{\rm ZPE}({\rm II}) \; . \tag{4.4}$$

3. Since the ice II $\rightarrow$ ice Ic transformation occurs at ambient pressure in the experiments, the contribution of the pV-term in the Gibbs free energy related to the density decrease during the transformation is negligible. On the other hand, $T \gg 0\,{\rm K}$ and so the temperature dependence of the vibrational contribution to the Gibbs free energy cannot *a priori* be neglected:

$$F_{\rm phonon}(V,T) = \underbrace{\frac{1}{2} \sum_{\mathbf{q},b} \hbar\omega_{\mathbf{q},b}(V)}_{E_{\rm ZPE}} + k_{\rm B}T \sum_{\mathbf{q},b} \ln \left[1 - \exp\left(\frac{-\hbar\omega_{\mathbf{q},b}(V)}{k_{\rm B}T} \right) \right] \tag{4.5}$$

   Here $k_{\rm B}$ is the Boltzmann constant and $\omega_{\mathbf{q},b}$ is the phonon frequency at wavevector $\mathbf{q}$ for band b. This results in

$$\Delta\tilde{H}(T) = \Delta E_{\rm lat} \; + \; F_{\rm phonon}(T;{\rm I}) - F_{\rm phonon}(T;{\rm II}) \; , \tag{4.6}$$

4. Finally, the configurational entropy S_{conf} has been also accounted for that results from the number of possible microstates in the H-subnetwork of the ice. This also includes the temperature dependence to the enthalpies according to

$$\Delta H(T) = \Delta \tilde{H}(T) + T S_{\mathrm{conf}} \,. \tag{4.7}$$

The expression $R \ln(\frac{3}{2}) = 3.37\,\mathrm{J\,mol^{-1}\,K}$ for S_{conf} is used as given by Pauling [48] throughout in this work. This expression is based on the number of microstates allowed according to the Bernal-Fowler ice rules [6], where only one central water molecule and four tetrahedrally connected water molecules are considered. Considering the actual structure of ice Ih and using a more rigorous approach, the Pauling expression has been corrected to $R \ln(1.507) = 3.40\,\mathrm{J\,mol^{-1}\,K}$ [49–52]. In spite of neglecting long-range effects such as ring closures, the Pauling approach is accurate to better than 1% for all ice structures. This accuracy is much better than chemical accuracy aimed for here.

It is noted that $\Delta H(T = 0\,\mathrm{K}) = \Delta \tilde{H}(T = 0\,\mathrm{K}) = \Delta E_{\mathrm{lat}}^{\mathrm{ZPE}}$, i.e. Eqs. (4.4), (4.6) and (4.7) are identical at $T = 0\,\mathrm{K}$. Furthermore, Eqs. (4.2), (4.4), (4.6) and (4.7)) has been evaluated based on the quasi-harmonic approximation (QHA). For $T \gg 0\,\mathrm{K}$ this study thus accounts for the thermal expansion due to the dependence of ω_i on the unit cell volume. The QHA has been very successful to account for nuclear quantum effects in different ice phases [53, 54] and found to be very accurate for $T \leq 200\,\mathrm{K}$ for ice Ih and ice II [55].

Lattice energies without and with ZPE for ice Ih and ice II are listed in Table 4.2. E_{lat} is identical for H_2O and D_2O, whereas $E_{\mathrm{lat}}^{\mathrm{ZPE}}$ differs for both isotopologues. Within the experimental uncertainties both models reproduce the available data for E_{lat} and $E_{\mathrm{lat}}^{\mathrm{ZPE}}$ within $1.5\,\mathrm{kJ\,mol^{-1}}$, which is much better than chemical accuracy ($4.2\,\mathrm{kJ\,mol^{-1}}$).

Table 4.3 compiles the transition enthalpies for the ice II $\rightarrow$ ice Ih transition. Based on E_{lat} alone (given in the first column) the transition is calculated to be strongly exothermic, where q-TIP4P/F predicts a much stronger exothermicity than MB-pol (-1466 vs. $-801\,\mathrm{J\,mol^{-1}}$). This alone does not match the experiments, which are weakly en-

Table 4.1: Summary of the onset temperatures T_o and enthalpies ΔH for H_2O and D_2O samples obtained from DSC measurements for the ice II $\rightarrow$ ice Ic transition following different preparation routes.

				Isotope effect on	
Preparation method	Ice II	T_o (K)	ΔH ($J\,mol^{-1}$)	T_o (K)	ΔH ($J\,mol^{-1}$)
Bauer *et al.* [19]	H_2O	172 ± 1	$+33 \pm 11$	7.0 ± 1.4	-165 ± 38
	D_2O	179 ± 1	-132 ± 36		
Salzmann *et al.* [20]	H_2O	170 ± 2	$+48 \pm 9$	10.0 ± 2.2	-197 ± 51
	D_2O	180 ± 1	-149 ± 50		

dothermic in the H_2O case and weakly exothermic in the D_2O case (see Table 4.1). The exothermicity is significantly reduced when including the ZPE in $\Delta E_{\mathrm{lat}}^{\mathrm{ZPE}}$ (second column in Table 4.3). Yet, even after consideration of ZPE the transitions are still clearly exothermic for both models and both isotopes (between -561 and $-732\,J\,mol^{-1}$). q-TIP4P/F predicts a somewhat stronger influence of ZPE than MB-pol does. Also when including the vibrational correction in $\Delta\tilde{H}$ this picture does not change very much (third column in Table 4.3). In fact, the vibrational correction at 150 K is almost identical for both H_2O and D_2O. It amounts to about $2\,J\,mol^{-1}$ for the MB-pol model, and about $30\,J\,mol^{-1}$ for q-TIP4P/F. The closest match with experiment is reached when also including the Pauling correction for the configurational entropy in ΔH (last column in Table 4.3). After this correction the ice II $\rightarrow$ Ic transition is exothermic by $-105\,J\,mol^{-1}$ for the D_2O case and the MB-pol model. This is very close to the experimental value given in Table 4.1. However, the switch from endothermic to exothermic cannot be accounted for. Both models show the ice II $\rightarrow$ Ic transition to be slightly exothermic for the H_2O case, by $-57\,J\,mol^{-1}$ for the MB-pol model. This transition enthalpy is very close to zero, just like the experimental value, but on the exothermic side. Considering the accuracy with which both water models reproduce the lattice energies in Table 4.2, it is not surprising that they fail to predict the absolute transition enthalpies correctly. On the other hand, the difference that quantifies the isotope effect on the ice II $\rightarrow$ Ic transition introduces some cancellation of errors, which leads to a

Table 4.2: Lattice energies for ice Ih and ice II in $\mathrm{kJ\,mol^{-1}}$ as defined in Eqs. (4.1) and (4.2). Experimental values have been obtained by extrapolating experimental values for the vibrational frequencies back to 0 K and calculating the zero-point energy therefrom [56, 57].

	E_{lat}	$E_{\mathrm{lat}}^{\mathrm{ZPE}}$	
		H_2O	D_2O
ice Ih			
q-TIP4P/F	−59.782	−47.216	−49.885
MB-pol	−59.464	−46.756	−49.552
experiments	−58.82[a]	−47.341(15)[a,b]	−48.611(615)[b]
ice II			
q-TIP4P/F	−58.316	−46.621	−49.153
MB-pol	−58.663	−46.195	−48.975
experiments	−58.88(10)[a]	−47.400(100)[a]	

[a]ref. [57]; [b]ref. [56].

better agreement with the experimental value of $-180 \pm 20\,\mathrm{J\,mol^{-1}}$. The q-TIP4P/F model fares somewhat better, predicting an isotope effect of $-135\,\mathrm{J\,mol^{-1}}$ as opposed to $-48\,\mathrm{J\,mol^{-1}}$ in case of MB-pol. Since the configurational entropy is exactly the same and the vibrational correction is almost identical for H_2O and D_2O, they cancel each other when considering the differences of $\Delta\tilde{H}$ and ΔH, which thus yield essentially the same result as $\Delta E_{\mathrm{lat}}^{\mathrm{ZPE}}$. That is, the main reason for the isotope effect noticed in this work is ZPE.

4.4 Conclusions

In summary, this study reports calorimetry scans for the high-pressure phase ice II at ambient pressure. These scans feature (i) the transition to cubic ice (ice Ic) at $170 \pm 2\,\mathrm{K}$, (ii) the very subtle transition from ice Ic to hexagonal (ice Ih) near 210 K

Table 4.3: Energy differences for the ice II → ice Ih transition in $\mathrm{J\,mol^{-1}}$ as defined by Eqs. (4.3), (4.4), (4.6) and (4.7).

	ΔE_{lat}	$\Delta E_{\mathrm{lat}}^{\mathrm{ZPE}}$		$\Delta\tilde{H}(T = 150\,\mathrm{K})$		$\Delta H(T = 150\,\mathrm{K})$	
		H_2O	D_2O	H_2O	D_2O	H_2O	D_2O
q-TIP4P/F	−1466	−595	−732	−627	−762	−121	−256
Isotope effect		−137		−135		−135	
MB-pol	−801	−561	−612	−563	−611	−57	−105
Isotope effect		−51		−48		−48	

and (iii) melting of ice Ih at 273 K (not shown in Fig. 4.1). Upon deuteration the onset temperature of the ice II → ice Ic transition shifts to 180 ± 1 K. This shift of about 10 K is clearly a kinetic effect and reflects the fact that the transition is from kinetically stable ice II to metastable ice Ic at ambient pressure. The enthalpy associated with the transition changes sign upon isotope substitution, from an endotherm of $+40\,\mathrm{J\,mol^{-1}}$ in case of H_2O to an exotherm of $-140\,\mathrm{J\,mol^{-1}}$ in case of D_2O. This represents, to the best of our knowledge, the first observation of sign change upon isotope substitution, at least in the thermal study of ice phases. That is, our findings show how isotope effects may change stability and how a metastable material may become stable upon isotope exchange.

Lattice energy calculations based on two flexible water models (q-TIP4P/F and MB-pol) were carried out to explain this finding. The observed isotope effect on the enthalpy can be traced back to the difference of lattice energies including ZPE. ZPE alone results in a difference of $137\,\mathrm{J\,mol^{-1}}$ for the ice II → ice Ih transition for q-TIP4P/F, which is close to the experimental value of $180\,\mathrm{J\,mol^{-1}}$. By contrast, MB-pol shows a difference of only $50\,\mathrm{J\,mol^{-1}}$, clearly underestimating the ZPE. The vibrational contribution has been also considered at 150 K and the configurational entropy contribution related to the H-order in ice II and H-disorder in ice Ic. Both of these are important for obtaining good values on the absolute transition enthalpy for the ice II → ice Ic transition in H_2O. However, these effects are similar for D_2O and H_2O, and accordingly not of relevance

in explaining the isotope effect. Future water models are challenged to reproduce the experimentally observed sign change of the ice II $\rightarrow$ ice Ic transition enthalpy. It might be necessary to include zero-point energies of different ice phases directly in the construction of these models. This study suggests the isotope effects on the melting transition of ice Ih (6012 vs 6280 J mol^{-1}) and the isotope effects on the transformation from high-pressure ices II (see Table 4.1), VI [11] and XII [12] to ice Ic as benchmark data, for which reliable calorimetric studies are available for both D_2O and H_2O. The ice II$\rightarrow$ice Ic transition is particularly challenging because this polymorphic transition involves both entropy and enthalpy changes. They are both of similar size but opposed sign, and so it is highly challenging to reproduce whether an endotherm or an exotherm results in sum.

4.A Appendix

Table 4.4: Thermal expansion at $T = 150\,\mathrm{K}$ relative to $T = 0\,\mathrm{K}$ in percent as calculated according to the quasi-harmonic approximation (QHA). See main text and [45] for details.

	H_2O	D_2O
ice Ih		
q-TIP4P/F	0.05	0.08
MB-pol	0.24	0.31
ice II		
q-TIP4P/F	0.82	0.85
MB-pol	1.16	1.25

Table 4.5: Lattice energies for ice Ih in $\mathrm{kJ\,mol^{-1}}$ as defined in Eqs. (4.3) and (4.4). Experimental values have been obtained by extrapolating experimental values for the vibrational frequencies back to 0 K and calculating the zero-point energy therefrom [56, 57].

	E_{lat}	$E_{\mathrm{lat}}^{\mathrm{ZPE}}$	
		H_2O	D_2O
ice Ih			
q-TIP4P/F	−59.782	−47.216	−49.885
q-TIP4P/F (SPGC)	−59.645	−46.911	−49.600
MB-pol	−59.464	−46.756	−49.552
MB-pol (SPGC)	−59.390	−46.817	−49.609
experiments	−58.82[a]	−47.341(15)[a,b]	−48.611(615)[b]

[a]ref. [57]; [b]ref. [56].

Table 4.6: Energy differences for the ice II → ice Ih transition in $\mathrm{J\,mol^{-1}}$ as defined by Eqs. (4.3), (4.4), (4.6) and (4.7)

	ΔE_{lat}	$\Delta E_{\mathrm{lat}}^{\mathrm{ZPE}}$		$\Delta\tilde{H}(T=150\,\mathrm{K})$		$\Delta H(T=150\,\mathrm{K})$	
		H_2O	D_2O	H_2O	D_2O	H_2O	D_2O
q-TIP4P/F	−1466	−595	−732	−627	−762	−121	−256
Isotope effect		−137		−135		−135	
q-TIP4P/F (SPGC)	−1379	−290	−477	−662	−809	−156	−303
Isotope effect		−187		−147		−147	
MB-pol	−801	−561	−612	−563	−611	−57	−105
Isotope effect		−51		−48		−48	
MB-pol (SPGC)	−875	−622	−669	−673	−715	−167	−209
Isotope effect		−47		−42		−42	

4.5 References

1. G. Tammann, *Ann. Phys.* **308**, 161–194 (1900).
2. G. J. Wilson, R. K. Chan, D. W. Davidson, E. Whalley, *J. Chem. Phys.* **43**, 2384–2391 (1965).
3. J. E. Bertie, E. Whalley, *J. Chem. Phys.* **40**, 1646–1659 (1964).
4. E. D. Finch, S. W. Rabideau, R. G. Wenzel, N. G. Nereson, *J. Chem. Phys.* **49**, 4361–4365 (1968).
5. B. Kamb, W. C. Hamilton, S. J. LaPlaca, A. Prakash, *J. Chem. Phys.* **55**, 1934–1945 (1971).
6. J. D. Bernal, R. H. Fowler, *J. Chem. Phys.* **1**, 515–548 (1933).
7. S. Kawada, *J. Phys. Soc. Jpn.* **32**, 1442–1442 (1972).
8. J. E. Bertie, L. D. Calvert, E. Whalley, *J. Chem. Phys.* **38**, 840–846 (1963).
9. Y. P. Handa, D. D. Klug, *J. Phys. Chem.* **92**, 3323–3325 (1988).
10. C. G. Salzmann, I. Kohl, T. Loerting, E. Mayer, A. Hallbrucker, *Phys. Chem. Chem. Phys.* **5**, 3507–3517 (2003).
11. J. J. Shephard, C. G. Salzmann, *Chem. Phys. Lett.* **637**, 63–66 (2015).
12. C. G. Salzmann, E. Mayer, A. Hallbrucker, *Phys. Chem. Chem. Phys.* **6**, 1269–1276 (2004).
13. T. Loerting, M. Bauer, I. Kohl, K. Watschinger, K. Winkel, *et al.*, *J. Phys. Chem. B* **115**, 14167–14175 (2011).
14. E. A. Zheligovskaya, *Crystallogr. Rep.* **60**, 714–720 (2015).
15. J. J. Shephard, C. G. Salzmann, *J. Phys. Chem. Lett.* **7**, 2281–2285 (2016).
16. M. S. Elsaesser, K. Winkel, E. Mayer, T. Loerting, *Phys. Chem. Chem. Phys.* **12**, 708–712 (2010).
17. G. P. Johari, A. Hallbrucker, E. Mayer, *Nature* **330**, 552 (1987).
18. O Mishima, L. Calvert, E Whalley, *Nature* **310**, 393 (1984).
19. M. Bauer, M. S. Elsaesser, K. Winkel, E. Mayer, T. Loerting, *Phys. Rev. B* **77**, 220105 (2008).
20. C. G. Salzmann, P. G. Radaelli, J. L. Finney, E. Mayer, *Phys. Chem. Chem. Phys.* **10**, 6313–6324 (2008).
21. E. Long, J. Kemp, *J. Am. Chem. Soc.* **58**, 1829–1834 (1936).
22. T. M. Gasser, A. V. Thoeny, L. J. Plaga, K. W. Köster, M. Etter, *et al.*, *Chem. Sci.* **9**, 4224–4234 (2018).
23. V. Fuentes-Landete, K. W. Köster, R. Böhmer, T. Loerting, *Phys. Chem. Chem. Phys.* **20**, 21607–21616 (2018).
24. V. Fuentes-Landete, L. J. Plaga, M. Keppler, R. Böhmer, T. Loerting, *Phys. Rev. X* **9**, 011015 (2019).
25. S. Habershon, T. E. Markland, D. E. Manolopoulos, *J. Chem. Phys.* **131**, 024501 (2009).

26. A. H. Larsen, J. J. Mortensen, J. Blomqvist, I. E. Castelli, R. Christensen, *et al.*, *J. Phys.: Condens. Matter* **29**, 273002 (2017).
27. S. Plimpton, *J. Comput. Phys.* **117**, 1–19 (1995).
28. V. Babin, C. Leforestier, F. Paesani, *J. Chem. Theory Comput.* **9**, 5395–5403 (2013).
29. V. Babin, G. R. Medders, F. Paesani, *J. Chem. Theory Comput.* **10**, 1599–1607 (2014).
30. G. R. Medders, V. Babin, F. Paesani, *J. Chem. Theory Comput.* **10**, 2906–2910 (2014).
31. C. Lobban, J. L. Finney, W. F. Kuhs, *J. Chem. Phys.* **117**, 3928–3934 (2002).
32. A. D. Fortes, *Acta Cryst. B* **74**, 196–216 (2018).
33. M. Matsumoto, T. Yagasaki, H. Tanaka, *J. Comput. Chem.* **39**, 61–64 (2018).
34. B. G. Pfrommer, M. Côté, S. G. Louie, M. L. Cohen, *J. Comput. Phys.* **131**, 233–240 (1997).
35. K. Parlinski, Z. Q. Li, Y. Kawazoe, *Phys. Rev. Lett.* **78**, 4063–4066 (1997).
36. A. Togo, I. Tanaka, *Scripta Mater.* **108**, 1–5 (2015).
37. E. A. Engel, B. Monserrat, R. J. Needs, *Phys. Rev. X* **5**, 021033 (2015).
38. M. Taylor, E Whalley, *J. Chem. Phys.* **40**, 1660–1664 (1964).
39. J. Li, *J. Chem. Phys.* **105**, 6733–6755 (1996).
40. D. D. Klug, E. Whalley, E. C. Svensson, J. H. Root, V. F. Sears, *Phys. Rev. B* **44**, 841–844 (1991).
41. T. H. G. Carr, J. J. Shephard, C. G. Salzmann, *J. Phys. Chem. Lett.* **5**, 2469–2473 (2014).
42. M. Celli, L. Ulivi, L. del Rosso, *J. Phys. Chem. C* **124**, 17135–17140 (2020).
43. M. Chaplin, *Water Phase Diagram - Triple Points*, Accessed on July 31st, 2020.
44. International Association for the Properties of Water and Steam, "Revised Release on the Pressure along the Melting and Sublimation Curves of Ordinary Water Substance," tech. rep.
45. S. Rasti, J. Meyer, *J. Chem. Phys.* **150**, 234504 (2019).
46. D. R. Moberg, S. C. Straight, C. Knight, F. Paesani, *J. Phys. Chem. Lett.* **8**, 2579–2583 (2017).
47. D. R. Moberg, P. J. Sharp, F. Paesani, *J. Phys. Chem. B* **122**, 10572–10581 (2018).
48. L. Pauling, *J. Am. Chem. Soc.* **57**, 2680–2684 (1935).
49. J. Nagle, *J. Math. Phys.* **7**, 1484–1491 (1966).
50. B. A. Berg, C. Muguruma, Y. Okamoto, *Phys. Rev. B* **75**, 092202 (2007).
51. C. P. Herrero, R. Ramírez, *J. Chem. Phys.* **140**, 234502 (2014).
52. M. V. Ferreyra, S. A. Grigera, *Phys. Rev. E* **98**, 042146 (2018).
53. B. Pamuk, J. M. Soler, R. Ramírez, C. P. Herrero, P. W. Stephens, *et al.*, *Phys. Rev. Lett.* **108**, 193003 (2012).

54. K. Umemoto, E. Sugimura, S. de Gironcoli, Y. Nakajima, K. Hirose, *et al.*, *Phys. Rev. Lett.* **115**, 173005 (2015).
55. R. Ramírez, N. Neuerburg, M.-V. Fernández-Serra, C. P. Herrero, *J. Chem. Phys.* **137**, 044502 (2012).
56. E. Whalley, *Trans. Faraday Soc.* **53**, 1578 (1957).
57. E. Whalley, *J. Chem. Phys.* **81**, 4087–4092 (1984).